___

## 3. Prediction of sub-seismic faults and fractures - integration of 3D seismic data, 3D retro-deformation, and well data on an example of deformation around an inverted fault

### Abstract

In addition to seismically mapped fault structures, a large number of faults below the limit of seismic resolution contribute to sub-surface deformation. However, a correlation between large- and small-scale faults is difficult because of their strong variation in orientation. A workflow to analyse deformation over different scales is described here. Based on the combination of seismic interpretation, coherency analysis, geostatistical analysis, kinematic modelling, and well data analysis, we constrained the density and orientation of sub-seismic faults, and made predictions about reactivation and opening of fractures.

We interpreted faults in seismic and coherency volumes at scales between several km and a few tens of meters. 3D retro-deformation was performed on a detailed interpreted 3D structural model to simulate strain in the hanging wall at the time of faulting, at a scale below seismic resolution. The modelling results show that (1) considerable strain is observed more than 1 km away from the fault trace, and (2) deformation around the fault causes strain variations, depending on the fault morphology. This strain variation is responsible for the heterogeneous sub-seismic fracture distribution observed in wells. We linked the fracture density from well data with the modelled strain magnitude, and used the strain magnitude as a proxy for fracture density. With this method we can predict the relative density of small-scale fractures in areas without well data. Furthermore, knowing the orientation of the local strain axis we predict fault strike, and opening or reactivation of fractures during a particular deformation event.

### 3.1. Introduction

One of the most important questions that drives basin research is how deformation is accommodated, because it is very heterogeneous over time and space, and over a wide range of scales (e.g. Yielding et al., 1992; Gauthier and Lake, 1993; Pickering et al., 1996; Bonnet et al., 2001). Faulting plays an important role in the deformation of sedimentary basins. Large-scale sub-surface faulting is typically identified by the interpretation of 2D or 3D seismic data, whereas small-scale sub-surface faulting is identified by spatially-isolated 1D well data (e.g. McLeod et al., 2000; Meyer et al., 2002; Walsh et al., 2002; and Figure 3.1). Faulting at medium-scale (displacement between c. 30 m and a few dm) can usually neither be recognized on seismic data nor well data (e.g. Gauthier and Lake, 1993; Yielding et al., 1996). However, faulting at this medium-scale plays an important role in reservoirs: large individual reservoirs can be disrupted by faults that enhance fluid flow, or produce compartmentalized deposits due to cementation of fractures (e.g. Ferrill et al., 2000; Mauthe, 2003; Parnell et al., 2004). Displacement along faults can change the juxtaposition between sand and clay layers, for example, which can lead to clay smearing on fault surfaces and, therefore, to a reduction in fluid flow (e.g. Stewart, 2001). In contrast, fracture networks may act as conduits for diagenetic fluids, or even as reservoirs, like in the mudstones of the Bristol Channel (Cosgrove, 2001), or in the Devonian cherts of Parkland field, Canada (Packard et al., 2001). These examples show that faulting below the limit of seismic resolution (hereafter referred to as sub-seismic) can strongly control fluid flow, and therefore has a significant importance in hydrocarbon reservoirs, diagenetic ore deposits, and geothermal energy reservoirs.
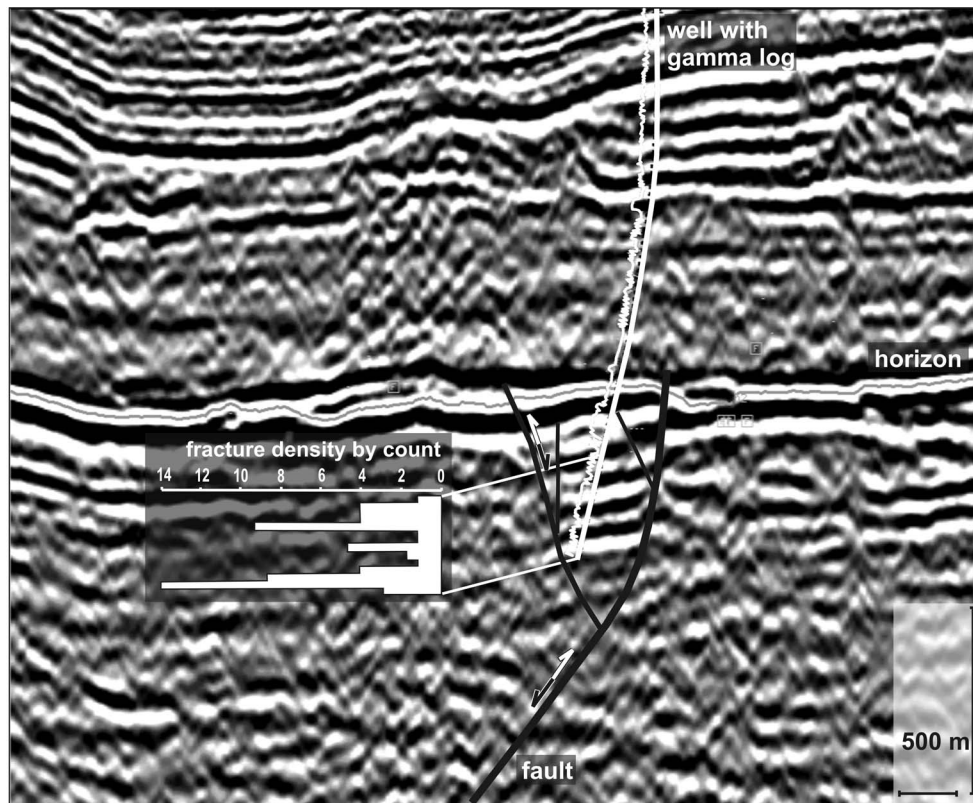
Figure 3.1: Information from seismic data set, from large-scale (seismic line with interpreted fault and horizon) to small-scale (well within hanging wall and corresponding gamma log, and fracture distribution from FMI data).

The key to understand the distribution and interaction of small- and medium-scale fractures lies in the evolution and kinematics of large-scale structures, because the dominant strain component is commonly accommodated by large-scale faults with offsets of several tens or hundreds of meters (e.g. Scholz and Cowie, 1990; Pickering et al., 1996; Ackermann and Schlische, 1997; Bonnet et al., 2001). Around these faults, smaller faults develop (for normal or inverted faults predominantly in the hanging wall, for thrust faults in both hanging wall and footwall), which accommodate minor strain with respect to the major fault. Nonetheless, the total amount of this sub-seismic strain can locally reach up to 50 % (e.g. Walsh et al., 1996; Schwarzer et al., 2003; Tanner et al., 2007, personal communication), but the precise position, orientation, or density variation of sub-seismic faults is difficult to estimate. However, knowing the 3D shape and the kinematic evolution of large-scale faults and their interaction, the surrounding fracture-network can be predicted.

The challenge is to develop a workflow that bridges the gap between large-scale 3D seismic data and small-scale 1D well data in order to make predictions about sub-seismic deformation in areas without well data (Figure 3.1). To identify the sub-seismic deformation, its magnitude and spatial distribution within 3D seismic data, and to make assumptions about fractures which were opened or reactivated during a particular deformation phase, we developed a workflow combining different methods of seismic data analyses, recently introduced by Krawczyk et al. (2006). For this purpose, we combine 3D kinematic modelling (retro-deformation) of horizons along large-scale faults, geostatistic analysis of medium-scale faults, and finally correlation of these results with small-scale fractures identified from well data. In a joint project the results discussed here are tied with the results from Trappe et al. (2007), who investigated the potential of geostatistical tools for fracture prediction.

## 3.2. Data base and reservoir characterisation

We analysed a pre-stack, depth-migrated 3D reflection seismic data set, provided by RWE Dea AG. The line spacing of the seismic volume is 25 m, with 25 m CDP binning and c. 30 m vertical resolution. The seismic data was interpreted with the Schlumberger software GeoFrame. Well data include information about fracture orientation from FMI data (Formation micro image), lithological information from core data and reports, as well as log data for correlation with the seismics (Figure 3.1).

Our study area is located within the NW German Basin. A detailed tectonic characterisation of the area can be found in Lohr et al. (2007). In our workflow, we concentrate on an area within a Rotliegend (Lower Permian) sandstone gas reservoir. The Permian is characterized by syn-sedimentary grabens and halfgrabens, in which well data documented mainly sandstone, but also fanglomerates and volcanic rocks. The Rotliegend sandstone reservoir is strongly fractured. These fractures cause problems in reservoir exploration and drilling prospects due to their cementation and the associated decrease in fluid flow and compartmentalization of the reservoir. Because of company confidentiality we avoid giving more detailed information of exact data location or orientation. Instead, assume that all maps, rose diagrams, and Schmidt nets shown here are orientated with North at the top.

## 3.3. Workflow

The suggested workflow includes several analyses of both seismic and well data on different scales (Figure 3.2). The four main parts of the workflow are presented in the four sub-chapters below.
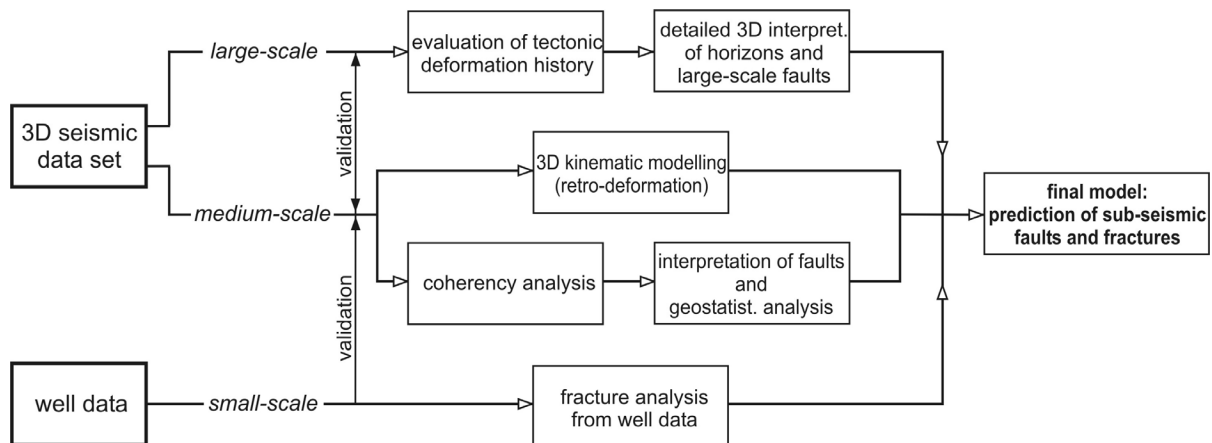


Figure 3.2: Flow diagram illustrating the developed workflow.

### 3.3.1 Tectonic deformation history

The first step in the workflow is the general investigation of the study area in terms of its geological evolution, and the comparison of these results with the regional evolution based on reflection seismic data. Here, the regional evolution encompasses sedimentation, faulting, and diapirism from Carboniferous to Tertiary times. On a regional scale, this is discussed in Lohr et al. (2007).
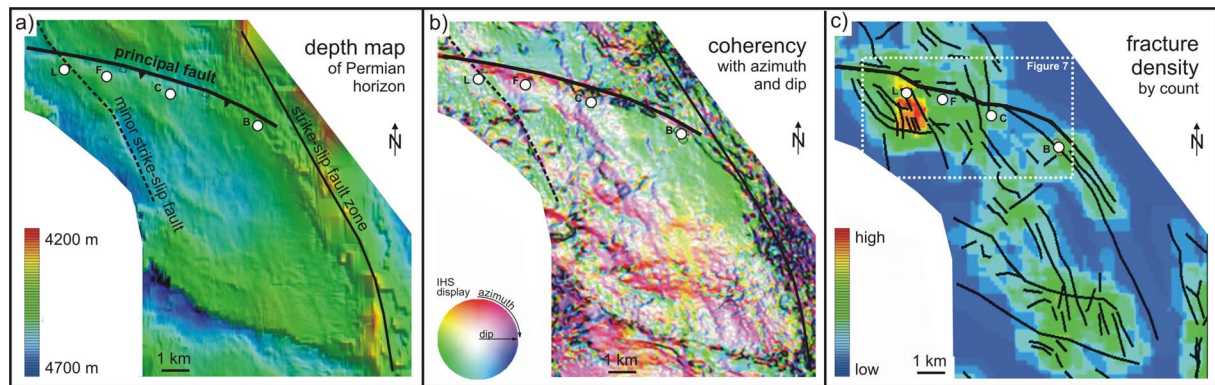
Figure 3.3: Top Rotliegend horizon in map view showing different attributes: (a) depth, (b) coherency with IHS display (intensity, hue, saturation) of dip and azimuth, and (c) interpreted faults with color-coded fracture density by count. The analyzed fault is indicated as "principal fault". The white circles label four wells (B, C, F, and L) penetrating the hanging wall.

The chosen example for the detailed study presented here consists of a 6 km long fault (principal fault in Figure 3.3) with a strongly deformed hanging wall (Figures 3.1, 3.3a). This Permian age normal fault was reactivated and inverted during the Cretaceous. Oblique to the principal fault, a strike-slip fault zone occurs (Figure 3.3a), that was initiated prior to Permian normal faulting and reactivated several times until the Tertiary (Lohr et al., 2007). Parallel to this strike-slip fault zone a subordinate strike-slip fault occurs that interacted with the principal fault (Figure 3.3a). We have chosen this example despite of the superposition of several deformation events, because here four wells have been drilled in the hanging wall of this relatively small structure, given the unique possibility to document the heterogeneous distribution of small-scale deformation.

The principal fault is slightly listric and is located at a depth between 4400 m (upper limit defined by end of deformation) and 5800 m (lower limit defined by seismic resolution). The principal fault, as well as the hanging wall and footwall were interpreted in 3D in detail (75 m grid for fault interpretation, 25 m grid for horizon interpretation). The triangulation of all surfaces was carried out using GoCad (GOCAD Consortium). The Midland Valley software 3Dmove was used to analyse the fault morphology, and to define kinematic parameters for the subsequent 3D kinematic modelling (retro-deformation).

## 3.3.2 Coherency analysis and geostatistical fault prediction

At a medium-scale, we analysed faults at the limit of seismic resolution using advanced coherency analysis. Two new coherency algorithms, "Structural Entropy" and "Shaded Relief" (Trappe et al., 2007), were developed to enhance subtle lineaments within 3D seismic data. The use of the advanced coherency algorithms significantly improved the quality of the attributes dip and azimuth, and therefore even subtle faults could be interpreted in detail (maximum resolution is about 9 m at that depth on horizon slices). To combine the medium-scale fault interpretation picked from the coherency volume, and the small-scale fracture analysis from well data, we performed a geostatistical fault analysis in order to test the reliability of both analyses. These methods and the interpretation results are described and discussed in Trappe et al. (2007).

Figure 3.3 shows the analysed horizon (Top Rotliegend) in map view as depth map (a), coherency map (b), and fracture density map (c) with fault pattern interpreted from (b) and seismic cross-sections. The color-coded fracture density is calculated by count. The resulting map demonstrates that fracture density is very heterogeneous, and that the highest fracture density occurs in the area close to well L (Figure 3.3).

_____

### 3.3.3  3D kinematic modelling (retro-deformation)

Figure 3.4 shows a 3D model of the analysed fault, the hanging wall, the footwall, and the position of four wells. Volumetric retro-deformation allows the backward movement of the hanging wall along the fault to a previous stage. In this manner, the hanging wall volume was retro-deformed along the 6 km long principal fault, and the resulting volumetric deformation of the hanging wall was used to predict the sub-seismic fractures occurring in this area. In our example, the inversion stage was retro-deformed by simulating extension (Figure 3.5). The calculation of hanging wall deformation during volumetric retro-deformation is based on the measurement of the translation of tetrahedrons within the hanging wall volume. This translation is strongly controlled by fault morphology. From the translation of tetrahedrons and the relative displacement of their nodes within the volume, 3Dmove calculates the strain tensor at each point of the deformed volume. Before discussing the results of volumetric deformation, we first introduce the parameters chosen for the modelling procedure, namely: the deformation algorithm, shear vector orientation, the amount of displacement, and the movement direction of the hanging wall.
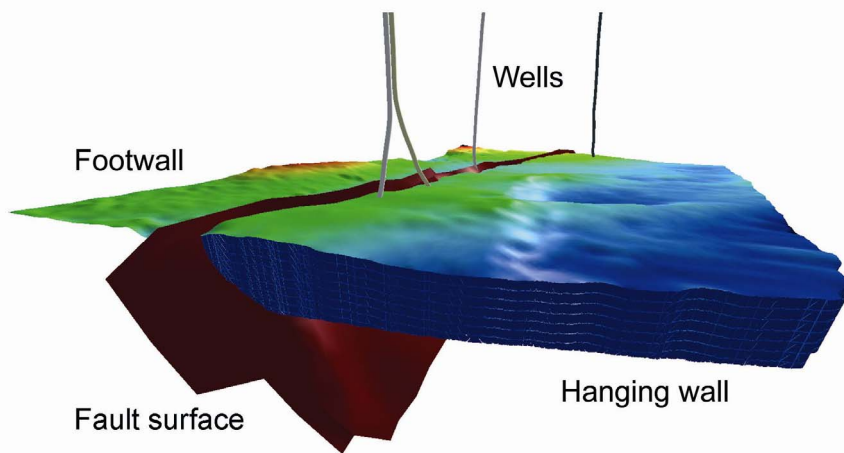


Figure 3.4: Present-day perspective view of the model illustrates the hanging wall volume, footwall, principal fault, and four wells. Hanging wall and footwall are color-coded by depth.

In 3Dmove, the "Inclined Shear" *deformation algorithm* was chosen. In contrast, other kinematic restoration algorithms in 3Dmove ("Flexural Slip" and "Fault Parallel Flow") use layer-parallel shear, suitable for simulation of contraction in fold and thrust belts. "Inclined shear" is used to model penetrative deformation resulting from movement over a fault plane, that occurs on a slip-system (within the hanging wall) oriented at an angle oblique to bedding (e.g. Gibbs, 1983; Suppe, 1983; Groshong, 1990; Withjack and Peterson, 1993). In the analysed seismic volume we observed antithetic faults within the hanging wall, which cut the bedding at an angle of c. 60°.

During retro-deformation the hanging wall moves along the fault. This movement is controlled by the *orientation of the shear vector*. An antithetic shear vector of 60° was used because of the presence of 60°-dipping antithetic faults within the seismic volume. These faults appear as discrete fault zones in the seismic volume, and can therefore be modelled as relatively stable large-scale shear zones.

The present-day observable separation of the footwall and hanging wall varies between 0 and 25 m along fault-strike. However, this amount does not represent the true displacement variation along fault-strike that occurred during inversion or extension, because of the superposition of both deformation events (Figure 3.5). For this reason, we did not incorporate this amount as a variable displacement in the deformation algorithm. Instead, we estimated from seismic data the *amount of displacement* that occurred during inversion to be about 100 m as a minimum value. The

_____

true amount of displacement cannot be measured more precisely since the amount of inversion was higher than the amount of extension, and since the analysed structure is relatively small to allow an identification of growth strata from the seismic data. However, an increase of displacement would lead to an increase of the strain magnitude, but for the modelling in this stage of the workflow only the relative magnitude of strain is important.
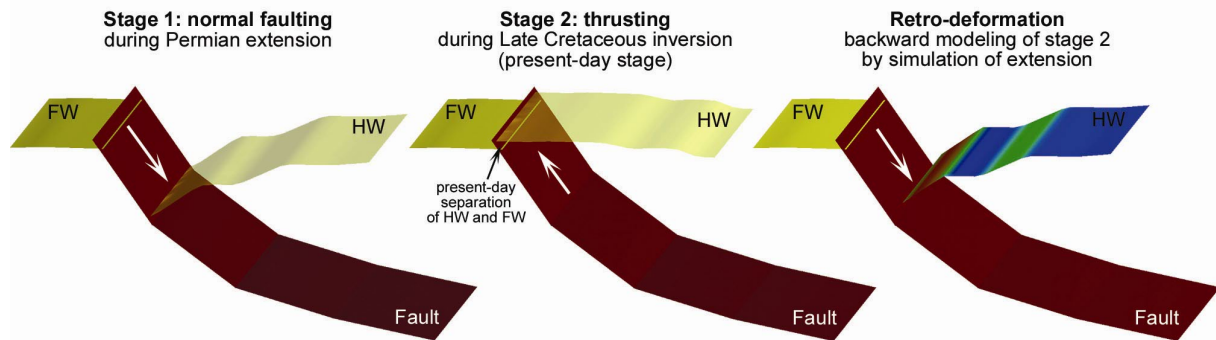


Figure 3.5: Schematic illustration of the method of retro-deformation, showing the two stages of deformation (extension, inversion). During retro-deformation the hanging wall is displaced downwards by simulation of extension. The white arrows indicate movement direction during the deformational stages. The color-coded hanging wall during retro-deformation indicates the strain of triangles (tetrahedrons in volumetric retro-deformation) within the deformed surface: red - high strain, green - medium strain, blue - low strain. FW - footwall, HW - hanging wall.

*Movement direction* was identified from fault morphology analysis by using attributes such as dip, azimuth, and cylindricity (Figure 3.6). These attributes highlight fault corrugations, which developed during fault-growth by segment linkage over time. The movement direction of the hanging wall is supposed to be parallel to the axis of these corrugations, which are perpendicular to fault strike in this example. Such corrugation-parallel movement requires least energy and therefore causes smallest strain within the hanging wall, rather than corrugation-oblique movement. Thus, the orientation of the fault corrugations can be used to define the movement direction on the fault (Needam et al., 1996).
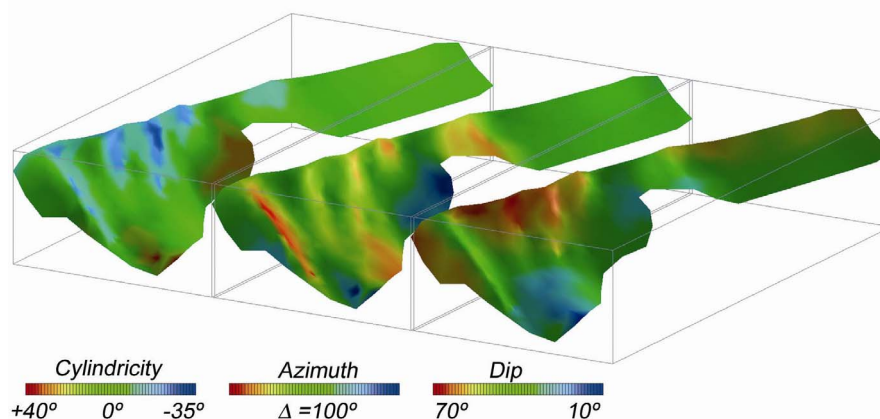


Figure 3.6: 3D view of the analyzed fault presenting three different attributes: dip, azimuth, and cylindricity. Fault length is 6 km, fault depth is max. 1.5 km. Dip and azimuth attributes show the dip and azimuth of each individual triangle of the fault-surface. Cylindrical analysis compares the orientation of the surface triangle normals with the orientation of the average cylindrical vector (parallel to surface-corrugations). A surface normal at 90° to the average cylindrical vector has a deviation attribute of zero. Deviations from this best-fit normal will have deviated attribute values above or below zero.
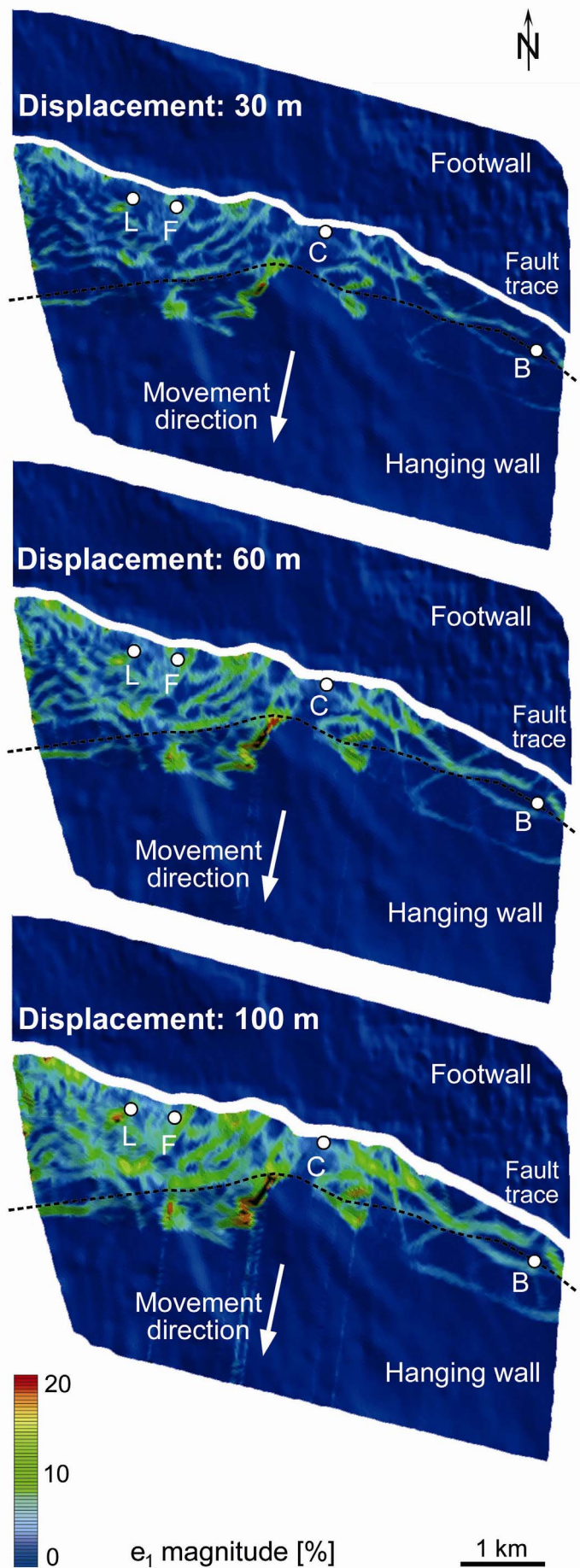
Figure 3.7: Results of 3D retro-deformation of model illustrated in Figure 4 are shown in map view after 30, 60, and 100 meter displacement. The magnitude of maximum strain ($e_1$) is colour-coded. Artefacts during modelling are related to the fault termination at depth. The dotted line marks the boundary between real modelling data (north) and artefacts (south).

_____

The definition of the required input parameters (deformation algorithm, shear vector, displacement, movement direction) for the retro-deformation is well constrained by the seismic interpretation. Nevertheless, we tested the influence of slight variations of these parameters finding similar results during modelling. Larger variations in the shear vector (more than +/- 20°) and in movement direction (more than +/- 10°) led to an abnormally high deformation of the hanging wall, and to an increased number of artefacts even after a few meters of displacement. Also, the use of other deformation algorithms, such as "Flexural Slip" and "Fault Parallel Flow", induced odd strain results. The effect of the amount of displacement was relatively low, still showing plausible deformation results up to a displacement of 300 m.

For the modelling applied in this study, we choose the following parameters: the deformation algorithm "Inclined Shear", a 60° antithetic shear vector, 100 m displacement, and corrugation-parallel movement direction. Figure 3.7 shows the model in map view at different steps during retro-deformation. The colour-coded maximum magnitude of strain increases with increasing displacement and ranges from 0 % to 20 % after 100 m displacement. The strain magnitude shows a strong heterogeneous spatial distribution, in both along fault-strike and along displacement directions. The highest deformation is observed in the West, whereas less deformation occurred in the East. Hanging wall deformation affects areas in larger distances of up to 1300 m from the fault. The locations of high-strain zones are stable throughout the deformation. However, these localized zones become broader with increasing displacement. Deformation of the hanging wall is strongly controlled by fault-morphology: Zones of similar strain magnitude do not only develop parallel to fault-strike as it would be the case during deformation on a planar fault-surface, but they are also curved, following the fault corrugations (Figure 3.7). In some areas they are even nearly perpendicular to fault-strike. Furthermore, the highest strain areas are located especially close to the fault in areas of strong changes in fault-strike or fault-dip.

### 3.3.4 Fracture interpretation from well data

Four wells have been drilled through the hanging wall of the principal fault (Figure 3.3), allowing a deformation analysis also at the small-scale of a few cm. FMI data of these wells were measured and provided by RWE Dea AG; the orientation of fractures is shown in Figure 3.8. The fracture planes **identified** in the four wells represent all fractures within the approx. 250 m thick sandstone reservoir. Within the reservoir, the number of fractures increases strongly from East to West with n = 9 in well B, and n = 270 in well L. The orientation of the fracture planes differ in all wells. Well B is characterized by steeply-dipping NW-striking fractures, whereas well C shows moderate to steeply-dipping, mainly NE-striking fractures. In well F a NW-striking fracture set can be identified, with scatters of other fracture orientations. Two main sets can be recognized in well L (for well L only a rose diagram was provided): steeply-dipping NW-striking faults, and moderately dipping NE-striking faults. Unfortunately, from FMI data alone it was not possible to distinguish between open and closed fractures in these wells.
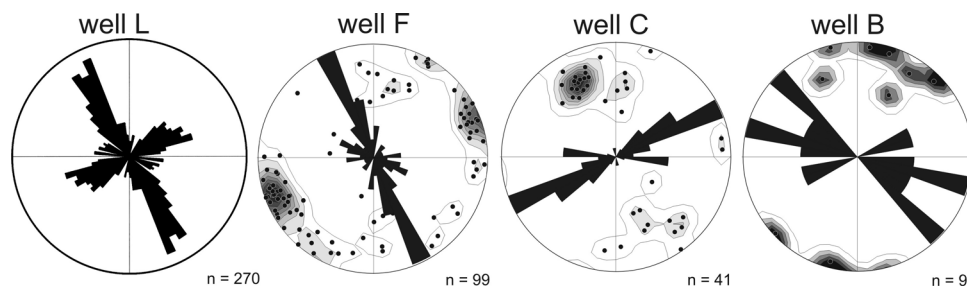


Figure 3.8: Fracture plots of FMI data, integrating both rose diagram (all wells; strike of fractures) and Schmidt net (well B, C, F; fractures planes are shown as pole points, plotted in equal-area stereonet, lower hemisphere projection). Well L: only rose-diagram is available. Number of fractures occurring within 250 m sandstone reservoir.

## 3.4. Discussion

### 3.4.1 Interpretation of modelling results

The strain data resulting from modelling describe the complete strain tensor, yielding magnitude, dip, and azimuth of all three principal strain axes ($e_1$, $e_2$, $e_3$, in which $e_1 > e_2 > e_3$, Figure 3.9) at any point of the tetrahedron. From the strain eigenvector information, we extracted the orientation of the maximum strain axis ($e_1$) for all data and for the data near each of the four wells and plotted them on a Schmidt net (Figure 3.10).
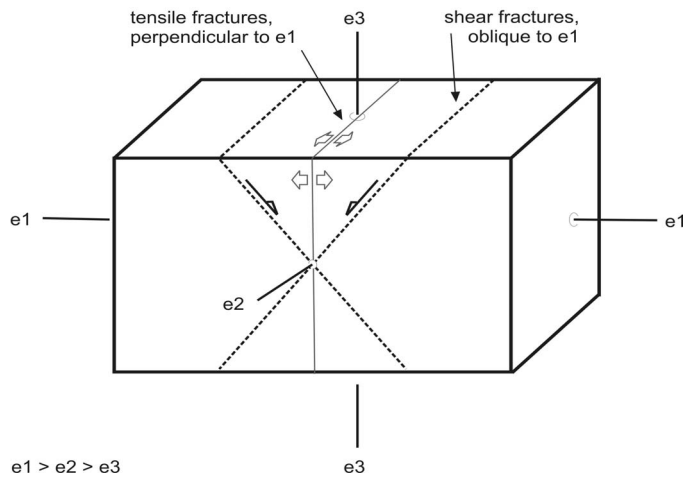


Figure 3.9: Sketch of the three strain axes ($e_1 > e_2 > e_3$) with possible orientation of tensile and shear fractures under extensional conditions, assuming isotropic rocks and non-rotational strain. Thereby, $e_1$ is used as an approximation for the maximum extension direction sigma 3, whereas $e_3$ is used as an approximation for the minimum extension direction sigma 1.
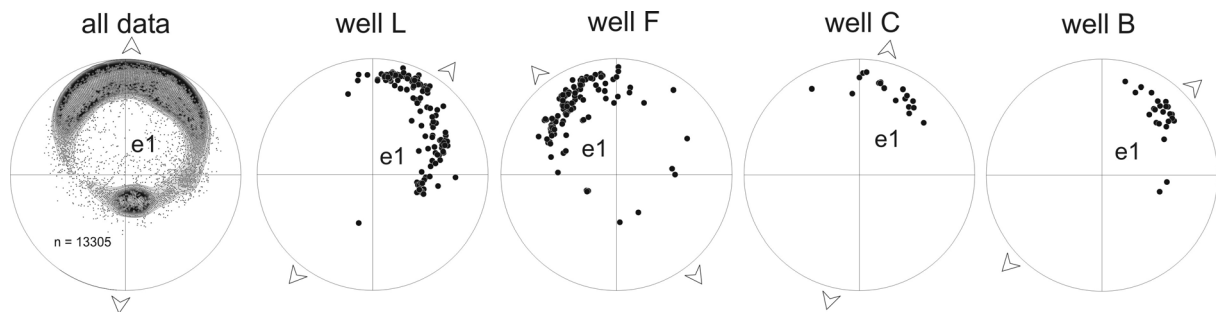


Figure 3.10: Maximum strain axis ($e_1$) around wells (extracted from a cylinder of about 400 m in diameter) derived from modelling shown in Figure 7. $e_1$ axes are shown as pole points, plotted in equal-area stereonet, lower hemisphere projection (Schmidt net). Arrows indicate the supposed max. horizontal extension direction derived from $e_1$ axes.

We assume that most of the strain in the study area occurs as brittle faulting. However, the real orientation of faults which developed during deformation cannot be completely reconstructed because of a lack of information about parameters influencing fracture behaviour, such as fluid pressure. The occurrence of fluids increases fluid pressure, which reduces the effective confining pressure and leads to shear or extension fractures, depending on the magnitude of differential stress (see Twiss and Moores, 1992). At small differential stresses, an increase in fluid pressure leads to extensional fractures, oriented perpendicular to $e_1$ (in this case $e_1$ represents the pole point to the fracture plane, Figure 3.9). At large differential stresses, an increase in fluid pressure leads to shear fractures of any orientation between 30° and 90° to the $e_1$ axis (Figure 3.9) depending on the amount of shear stress. Similar complexity may arise from fracture formation in an anisotropic rock or from reactivation of earlier fractures.

The $e_1$ axis can be used as an approximation for the maximum extension direction during the modelled deformation. By knowing the orientation of the $e_1$ axis at any location, it is possible to predict a preferred reactivation and opening of existing fractures and faults at this location.

The $e_1$ axes near the wells were extracted from the whole modelled data set (extracted from a cylinder of about 400 m in diameter), and their orientation is shown in the Schmidt net (Figure 3.10). The orientation of the $e_1$ axes of the whole data set is also given. The majority of the summarized axes plunges towards the N, with a variation from NW to NE, equivalent to fracture planes striking parallel to the principal fault plane. This variation is caused by local differences in strike due to the undulation of the fault surface. Another smaller cluster of e1 axes shows the same strike of fractures, but dips in the opposite direction, and therefore may represent the conjugate part of the main fracture set. The orientation of the axes varies strongly between the wells. Wells B, C, and L are characterized by mainly NE plunging e1 axes, whereas the e1 axes of well F plunge towards the NW. For the modelled deformation the maximum horizontal extension direction was N-S, but local extension varies around 90°, from NW-SE to NE-SW (Figure 3.10). Since retro-deformation is the reverse of forward-deformation, the local maximum horizontal extension direction for retro-deformation is equivalent to the local maximum horizontal compression direction for forward-deformation.

## 3.4.2 Comparison between coherency, modelling, and well data

The comparison of FMI, modelling, and coherency data is shown in Figure 3.11. Here, fractures from FMI data are compared with faults from the interpretation of coherency data and fault zones (corresponding to high-strain areas) derived from tectonic modelling. The rose diagrams of each well show the strike of all fractures identified from FMI data, as well as the local maximum horizontal compression direction estimated from the orientation of the modelled e1 axes (c.f. Figure 3.10). Of all fracture data shown in Figure 3.10, the red- and blue-coloured once are those that correspond in orientation to faults or fault zones that have been identified from coherency analysis and modelling respectively. Both those predicted fault patterns match in some parts, especially in areas where they are sub-parallel to the principal fault (Figure 3.11); however in most other areas the fault patterns do not match. This is mainly caused by the different scales the faults have been interpreted/modelled, and the different methods that have been used. While fault interpretation occupies all deformation events in the coherency data, the tectonic modelling considers only one deformation event.

Around *well L* the NW-striking fractures seen in the rose-diagram have been recognized by coherency analysis, whereas the NE-striking fractures have been recognized by modelling (Figure 3.11). The NE-striking fractures are oriented nearly parallel to the proposed maximum horizontal compression direction, and are therefore appropriate to have opened during inversion.

The NW-striking fractures around *well F* have been identified with coherency analysis, but the NE-striking fractures identified from modelling are only of minor presence in the well data. The local compression direction is parallel to the NW-striking fractures, so that these have possibly opened during inversion.

The strike of fractures in *well C* is mainly NE, but these fractures could be recognized neither by coherency analysis nor by modelling. However, a minor WNW-striking fracture set observable in well C has been recognized by modelling. Another fracture set recognized by coherency analysis could not be confirmed by the well data. The proposed orientation of compression direction during inversion is about 50° to the strike of fractures, and therefore does not refer to a likely opening of existing fractures.
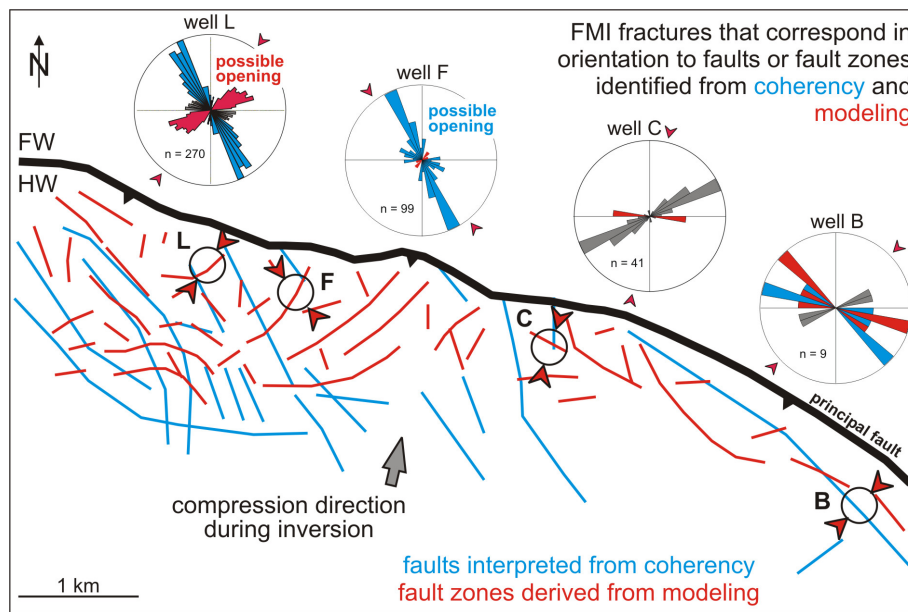
Figure 3.11: Map shows the principal fault with hanging wall deformation: red-colored structures are fault zones corresponding to high-strain areas that have been derived from modelling (Fig. 3.7); blue-coloured structures are faults that have been interpreted by coherency analysis (Fig. 3.3). Fracture plots show all FMI data of the four wells. In colour are fractures that have been identified also by modelling (red) or coherency analysis (blue). Small red arrows around plots and in the strain map around well locations demonstrate the local stress deviations derived from modelling, whereas the large grey arrow marks the superimposed maximum horizontal compression direction active during inversion. FW - footwall, HW - hanging wall.

Around *well B*, we detected NW-striking faults by both coherency analysis and modelling. This orientation corresponds to fractures detected in well data. A NE-striking fracture set can be noticed only in well data; however, this fracture set consists of only two fractures and is thus underrepresented. The orientation of the NE-striking fracture set in well B is not appropriate to have opened during inversion, as it has an angle of about 70° to the maximum horizontal compression direction (Figure 3.11).

Most of the fracture orientations measured in the analysed wells have been identified either with coherency analysis (wells L, F) or modelling (wells L, F, C), or with both (well B). Well C is the only well, in which the major fracture set could not be recognized with any of the two methods (Figure 3.11). In general, the faults that have been identified by modelling are those, which belong to the inversion event. Faults that have been identified by coherency are those, which belong to any of the three deformation events (extension, inversion, strike-slip faulting). Since the majority of former extensional faults have been reactivated during inversion, we distinguish only between dip-slip faulting (extension and inversion) and strike-slip faulting.

We interpret the fractures observed around well B to belong to the extension/inversion deformation. The fractures observed around wells L and F belong to the extension/inversion deformation when they were recognized by modelling (NE-striking structures), and to the strike-slip deformation when recognized by coherency analysis (NW-striking structures). In this area (wells F, L) the extension/inversion event has not been detected by coherency interpretation, possibly because the strike-slip faults are dominant and superimpose the others. In the FMI data, the predicted NE-striking extension/inversion structures are underrepresented, which is caused by either the incomplete detection of these fractures by the FMI method, or by an inaccuracy in modelling (e.g. incorrect fault surface interpretation due to superposition of strike-slip faults in

_____

this area). A possible explanation for the missing detection of NE-striking faults around well C by coherency analysis and modelling may be that these structures have probably initiated during extension, but have not been reactivated during inversion. Alternatively, they are below the resolution of coherency analysis.

Deformation during inversion along the principal fault can lead to reactivation and re-opening of pre-existing faults (normal faults, strike-slip faults), especially in areas where the orientation of the local stress field is suitable (Figure 3.11). The here proposed opening of fractures (in wells L and F) refers only to the modelled deformation event (inversion). Due to the subsequent influence of strike-slip faulting, the predicted opening of fractures is not necessarily a present-day prediction. The example studied here is complicated because of the superposition of two different fault patterns during three deformation events, which led to an accumulation of fracture density in the area of the wells F and especially L, because here strike-slip faulting is most prominent.
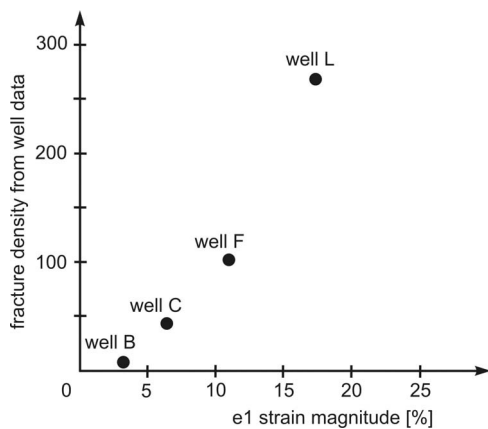


Figure 3.12: Diagram showing the fracture density of well data against $e_1$ strain magnitude derived from modelling. For discussion see text.

With respect to the modelled deformation it is possible to estimate the fracture density in the study area. By assuming that the fracture density increases with increasing strain magnitude, we can link the fracture density from FMI data with the strain magnitude from modelling for the same area, and use the strain magnitude as a proxy for fracture density at any given region within the modelled area. The diagram (Figure 3.12) shows the fracture density of all wells plotted against the maximum strain magnitude. The relation between both parameters demonstrates a positive trend, but a quantitative correlation cannot be done, because the fracture development also depends on material parameters such as rheology, porosity, fluids, or anisotropy, and on their spatial variation. Additionally, due to the influence of strike-slip faulting in the area of well F, and especially well L, the fracture density is slightly increased because it was not included in the modelling. However, even with these limiting parameters, there is a positive trend between fracture density and strain magnitude, which can therefore be used as a first qualitative estimation for fracture density within the study area.

### 3.4.3 Applications

Our results show strain variations along the principal fault, because strain is related to the fault shape. When moving along the fault, the hanging wall undergo penetrative deformation caused by the fault morphology, which results in local strain variations. Local maximum strain axes differ by as much as 90°. The strike variations of secondary faults are the result of these strain variations, which are caused by stress perturbations around the principal fault. These variations do not need to be explained by other tectonic events or reactivated older structures. Strain variations are important when using data such as kinematic indicators and fracture orientation

from field data, to estimate the regional stress field. These local data can differ strongly, and therefore do not necessarily represent the superimposed regional stress field.

With the proposed workflow, combining different methods at different scales (see also Krawczyk et al., 2006), we are able to estimate the fracture density and orientation in future prospects, and to make assumptions about fractures, which have been opened or reactivated during a particular deformation event. By knowing the position of high-strain zones predicted by modelling, it is also possible to assess fault connectivity and fluid flow. These qualitative strategies result in an improved evaluation of the reservoir quality. However, this workflow is particularly appropriate for reservoirs which are fracture-controlled, and where the fractures need to be identified, either in case of open fracture networks, which enhance fluid flow, or when cemented fractures reduce fluid circulation.

The workflow does not consider heterogeneous sedimentology or variable diagenetic processes, as it is the case in many reservoirs. These parameters need to be considered in the future as they interact with each other and play an important role for reservoir characterization. Other limitations of this study are given by the multiphase tectonic history, including extension, inversion, and in addition strike-slip faulting, which complicates the modelling results. Modelling of a structure which underwent only one deformation event would result in a more precise comparison of the fault pattern between coherency and modelling data, and less ambiguous results in terms of density and orientation of fractures, as well as in opening/closure predictions. However, the advantage of having four wells along a relatively small structure makes the working area useful for this kind of analysis. Therefore, we suggest that the workflow introduced here is a helpful tool for understanding sub-seismic deformation. It can be used as an additional reservoir modelling tool for the prediction of small-scale faults and fractures (in particular their orientation, density, and connectivity), which is important for identifying compartmentalisation and fracture networks, and finally contribute to improving fluid flow simulations and well placement.

## 3.5. Conclusions

The heterogeneous fracture pattern observed in well data cannot be explained by large-scale seismic interpretations alone. Resolution and identification of small-scale fractures and faults is possible and feasible with the combined method of detailed coherency analysis and 3D retro-deformation. To get the most information out of the seismic data, we compared the modelling results with detailed fault interpretations on attribute data from coherency horizon slices, and with fracture orientations from well data. Despite the modelling limitations in terms of spatial variation of sedimentological features, rheological parameters, and variable diagenetic processes, the comparison of modelling and coherency results with well data reveal a correlation, and provide an explanation for the disparate fracture pattern by comparing well data and seismic data directly.

The modelling is based on a clear definition of a major large-scale fault in 3D and the temporal and kinematic understanding of its deformation. Our results demonstrate that deformation around a fault causes strain variations depending on the fault morphology. Strain variations around a larger fault result in differences in fracture orientation at a smaller scale. The angle between the regional and the local strain axis can differ up to 90°. The identification of strain variations over several scales helps to predict the orientation and relative density of fractures in areas without well data, and to assess opening or reactivation of fractures during deformation.

_____

Our results show that these methods (3D retro-deformation, coherency analysis) integrated in the suggested workflow, are a powerful tool that bridges the gap between large-scale 3D seismic data and small-scale 1D well data for prediction of sub-seismic deformation.